Optically Induced Forces Imposed in an Optical Funnel on a Stream of Particles in Air or Vacuum

Niko Eckerskorn,[1] Richard Bowman,[2,3] Richard A. Kirian,[4,5] Salah Awel,[4,7] Max Wiedorn,[4,6] Jochen Küpper,[4,6,7] Miles J. Padgett,[2] Henry N. Chapman,[4,6,7] and Andrei V. Rode[1*]

[1]*Laser Physics Centre, Research School of Physics and Engineering, The Australian National University, Canberra, Australian Capital Territory 2601, Australia*
[2]*SUPA, School of Physics and Astronomy, University of Glasgow, Glasgow G12 8QQ, United Kingdom*
[3]*Nanophotonics Centre, Cavendish Laboratory, University of Cambridge, Cambridge CB3 0HE, United Kingdom*
[4]*Center for Free-Electron Laser Science, DESY, 22607 Hamburg, Germany*
[5]*Department of Physics, Arizona State University, Tempe, Arizona 85287-1504, USA*
[6]*Department of Physics, Universität Hamburg, 22761 Hamburg, Germany*
[7]*Center for Ultrafast Imaging, Universität Hamburg, 22761 Hamburg, Germany*

(Received 27 August 2015; revised manuscript received 29 October 2015; published 11 December 2015)

Optical trapping of light-absorbing particles in a gaseous environment is governed by a laser-induced photophoretic force, which can be orders of magnitude stronger than the force of radiation pressure induced by the same light intensity. In spite of many experimental studies, the exact theoretical background underlying the photophoretic force and the prediction of its influence on the particle motion is still in its infancy. Here, we report the results of a quantitative analysis of the photophoretic force and the stiffness of trapping achieved by levitating graphite and graphite-coated glass shells of calibrated sizes in an upright diverging hollow-core vortex beam, which we refer to as an "optical funnel". The measurements of forces are conducted in air at various gas pressures in the range from 5 mbar to 2 bar. The results of these measurements lay the foundation for mapping the optically induced force to the intensity distribution in the trap. The mapping, in turn, provides the necessary information to model flight trajectories of particles of various sizes entering the beam at given initial speed and position relative to the beam axis. Finally, we determine the limits of the parameter space for the particle speed, size, and radial offset to the beam axis, all linked to the laser power and the particular laser-beam structure. These results establish the grounds for developing a touch-free optical system for precisely positioning submicrometer bioparticles at the focal spot of an x-ray free-electron laser, which will significantly enhance the efficiency of studying nanoscale morphology of proteins and biomolecules in femtosecond coherent diffractive imaging experiments.

DOI: 10.1103/PhysRevApplied.4.064001

I. INTRODUCTION

Optically induced forces provide a promising route to touch-free guiding of airborne particles of micrometer and submicrometer sizes [1–5]. In general, there are two types of forces responsible for the impact of laser light on light-absorbing particles suspended in a gaseous environment. The first is the force of light pressure due to momentum transfer by photons. The broad field of optical trapping was pioneered by Ashkin [6], who in his first demonstration proposed and developed the basic concept of a counter-propagating gradient-force optical trap. In his experiments, he established that the radiation pressure from a continuous-wave laser beam of a few tens of milliwatts could stably hold micrometer-sized dielectric particles in a three-dimensional confinement in air and in vacuum.

The second force is a thermal or photophoretic force F_{PP}, which results from the transfer of momentum from gas molecules to the particles and occurs only if the surface of a particle is unevenly heated by an incident light beam. Under anisotropic heating, surrounding gas molecules rebound off the surface with different velocities creating a net force on the particle [7]. This effect was discovered by Ehrenhaft [8] a century ago and termed *photophoresis*. It depends on the particle size relative to the mean free path of gas molecules and, thus, on the gas pressure, the absorption of laser light, and thermal conductivity of the particle [9–11]. The ratio of the gas mean free path to particle diameter is known as the Knudsen number Kn. The force experienced by an irradiated surface depends on gas pressure p in the following way: F_{PP} is directly proportional to p at extremely low pressures, inversely proportional to p at extremely high pressures, and the plot of F_{PP} over a logarithmic pressure scale is symmetric with respect to the characteristic pressure at which $\mathrm{Kn} \sim 1$ where F_{PP} attains a maximum as illustrated

*Corresponding author.
andrei.rode@anu.edu.au

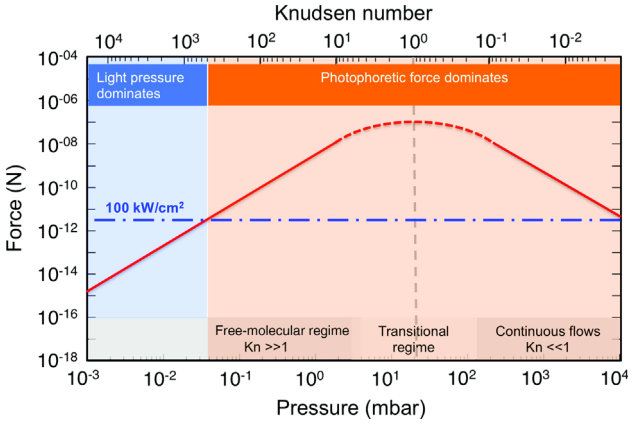

FIG. 1. Illustration of the dependence of photophoretic force (red line) on gas pressure for different regimes of Knudsen number Kn. The force is calculated for a highly absorbing 1-μm-diameter particle, for which the Kn ~ 1 at approximately 20 mbar. In the continuum-flow regime (Kn $\ll 1$), the force increases with reduced pressure, followed though the transition area Kn ~ 1 into the free-molecular regime (Kn $\gg 1$) where the force reduces with reduced pressure. The point where photophoretic force equates with the force of light pressure depends on the illumination intensity. We show, as an example, that at 100 kW/cm^2, the force of light pressure imposed on a 1-μm particle is equal to approximately 3 pN, so the light-pressure force dominates at pressures below 4×10^{-2} mbar.

in Fig. 1 [12,13]. Photophoretic forces can be up to 3 orders of magnitude higher than the radiation pressure at normal atmospheric conditions [3].

The value of photophoretic force is characterized by a Knudsen number Kn. The mean free path for the gas molecules at normal conditions in air is approximately 94 nm and varies inversely with pressure. In the free-molecular-flow regime, where particles are much smaller than the mean free path (Kn $\gg 1$), the photophoretic force can be estimated by kinetic theory in which case-reduced pressure results in smaller forces [9–11]. In the continuous regime (Kn $\ll 1$), the nature of the interaction has a very different mechanism: the particle's motion is due to the thermal creep phenomenon resulting from the particle-surface-temperature distribution [12–14]. In this regime, the force increases when the pressure is reduced and can be modeled using the equations governing continuous gas media with proper slip-flow boundary conditions. Thermal creep is a rarefaction effect, which occurs due to gas microflow along the walls with heat flux and depends on the temperature gradient of the gas along streamlines [9]. It is temperature driven, not pressure driven, as the gas moves in the direction of increasing temperature. The temperature difference, in turn, depends on the particle absorption for the laser light, which is wavelength dependent and on the thermal conductivity of the particle. In all the above conditions, the momentum transfer for a light-absorbing particle is in the direction from hot to cold; thus, the particle moves away from regions of high illumination intensity.

A solid theoretical background to predict the photophoretic force in the transitional regime Kn ~ 1 is still elusive [9,11–13]. To date, there is no theory unifying laser trapping by both radiation force and photophoretic force, and there is no united approach that covers the transitional range Kn ~ 1 of particular interest for trapping and transport of macromolecules [13,14] and indeed the range of interest for this work. For a particle size of approximately 1 μm, Kn ~ 1 is reached at about 20 mbar (see Fig. 1). At lower gas pressures, the photophoretic force decreases and at some point becomes lower than the light-pressure force. We indicate this pressure of 0.04 mbar in Fig. 1 for a 1-μm particle by taking, somewhat arbitrarily, a 3-pN force from the pressure of light.

In the Kn $\ll 1$ regime with small particles at atmospheric pressure, both radiation pressure and photophoretic forces are linearly dependent on the incoming laser intensity, and both push the light-absorbing particles toward the direction of the beam propagation and from higher-intensity to lower-intensity illumination. The repulsion from the high-intensity area is the reason why it is difficult to trap absorbing particles with a Gaussian beam profile [15], where the position at the maximum of beam intensity is unstable and particles are pushed away from the beam axis. An obvious solution to the problem is the use of structured beams with a doughnut intensity profile such as vortex beams, initially proposed by He *et al.* [16] and Rubinsztein-Dunlop *et al.* [17] for use in optical tweezers to handle light-absorbing particles with tightly focused beams in liquid media. Specifically, the laser vortex beam traps the particle on the axis where the incident intensity is minimal. The particle on the axis is in stable equilibrium because a small transverse perturbation increases the illuminating intensity and forces push it back to the axis. Optical vortices serve not only as a microscopic tool that can not only hold micrometer-size particles at rest or translate them in liquid media but also rotate them about the beam's axis. A large variety of laser beams with complex architecture offered a high level of stability and robustness to trapping [18–20]. The first use of optical vortices for trapping and transporting light-absorbing particles in air was demonstrated using counterpropagating coaxial vortex beams [21,22]. Following this work, the effect of polarization on the trap in linear and spatially variant polarized vortex beams is investigated [23,24].

The optical positioning and long-distance transport of absorbing particles in a gaseous environment or in vacuum opens up a previously unattainable domain of optical manipulation suggesting diverse new applications. Several optical schemes based on various beam architectures with minimum-intensity field were proposed to trap particles in gaseous environments since the first demonstration. Among those are selective trapping of thousands of particles in randomly distributed pockets of a speckle field [25,26], synchronous manipulation of particle ensembles using an

optical lattice formed by multiple-beam interference [27], trapping particles in a tapered-ring optical trap diffracted from a circular aperture [28], and in a bottle beam generated using a moiré technique [29]. Optical trapping can also be applied in robust 3D manipulation of particles using an optical bottle formed inside the focal volume of a lens with a controlled amount of spherical aberration [4,30] or through holographic-based schemes [31]. Besides trapping in 3D, the control of particle trajectory and speed is also important for delivering particles to measurement apparatuses for morphology and composition studies. Such techniques include a diverging quasi-Bessel beam [32] and/or an air-filled photonic-crystal fiber [5,33].

The present study is motivated by single-particle diffractive imaging at an x-ray free-electron laser (XFEL). XFELs are among the latest generation of x-ray sources and are unique in their ability to produce few-femtosecond-duration pulses of few-millijoule pulse energy. Remarkably, XFELs can combine atomic-spatial-resolution imaging with femtosecond temporal resolution. Single-particle diffractive imaging is an especially enticing possibility that is enabled by XFELs. This methodology typically consists of delivering a stream of isolated nanoparticles (such as proteins and viruses) across the intense focus of the pulsed, few-femtosecond-duration XFEL beam. Through the aggregation of diffraction patterns from a large number of individual particles, three-dimensional electron-density maps can be formed without prior knowledge of the particle structure, and time-resolved studies can be enabled through, for example, an optical pump pulse that precedes the delayed x-ray probe pulse. At present, one of the key bottlenecks in single-particle data collection at XFELs is the small size of the 100-nm-diameter x-ray beam [34] in comparison to an aerodynamically focused particle stream of a few tens of micrometers [35]. This mismatch between the particle stream size and x-ray beam size results in low sample delivery efficiency—only about one in 10^{12} particles are intercepted in the case of a 50-μm particle beam moving at 200 m/s across a 100-nm x-ray beam. As a result, many samples, which are often precious, are wasted, and days of data collection are often required in order to obtain only a few hundred or perhaps 1,000 high-quality diffraction patterns at an x-ray pulse repetition rate of 120 Hz, whereas $>100\,000$ patterns are required for atomic-resolution imaging [36].

In the context of single-particle imaging, optically induced forces are appealing due to their ability to enable a level of "touch-free" positioning precision that, so far, has not been achieved through aerodynamic focusing schemes. Our proposed scheme employs a diverging optical vortex beam as an "optical funnel" to compress and slow down a spray of fast-moving aerosolized particles initially formed by an aerodynamic lens [35]. The aerodynamic lens [35] produces a nearly collimated beam of particles with a beam diameter and speed depending on the size of the particle. Smaller particles tend to move faster (up to about 400 m/s for 10-nm particles) and produce larger beams when compared to bigger particles. Reducing the particle beam diameter and/or particle speed can increase the fraction of x-ray pulses that intercept a particle. For instance, a 1-μm particle beam moving at 1 m/s will reduce the data-collection time by a factor of about 10 000 when compared to a typical beam of 50 μm diameter and 200 m/s speed. The difficulty in predicting the magnitude of optically induced forces is complicated by the fact that the aerosol injector produces particles suspended in a mixture of both the carrier gas and water vapor, which undergoes rapid expansion into a vacuum chamber maintained at approximately $10^{-1} - 10^{-6}$ mbar. While most of the water from the initial mist of particle-laden microdroplets evaporates prior to reaching the vacuum chamber, the exact residual pressure and concentration of water vapor in the area near the injector nozzle is typically unknown and uncontrolled, and the gas density and velocity field at the x-ray interaction point are not well characterized. For this reason, the prediction of the force can, at this point, be made only from model experiments, where the upper level of the optical force is limited by a photophoretic force at atmospheric pressure, and the lower limit is due to the radiation pressure in vacuum. Clearly, considerable empirical investigation of the optical force acting on the particles in the diverging doughnut-shaped laser beam is required to predict the beam intensity and divergence required to effectively confine the injected particles into the few-micrometer-size x-ray focus.

As an important step toward achieving our ultimate goal, we calibrate the optical force imposed by the diverging vortex beam by levitating absorbing particles of various micrometer-size graphite and graphite-coated glass shells at a broad range of laser power and air pressure. We recover the axial force from the known particle mass and the radial force by measuring stiffness of trapping in the transverse plane and the standard deviation of the particle displacement from the equilibrium position at the beam axis due to the Brownian motion in the static levitating conditions. Furthermore, for the known laser-illuminating conditions, we predict the trajectories of the particles entering the diverging vortex beam with various speed, size, and distance away from the beam axis. The determined laser parameter space allows us to lay a foundation for a high-precision, touch-free, optical delivery system for pinpoint injection of submicrometer particles into a micrometer-size focus of an x-ray free-electron laser.

II. LEVITATING PARTICLES IN A DIVERGING VERTICAL VORTEX BEAM

A. Light-induced force on a spherical particle

1. Experimental setup

The particle trap is formed by a diverging beam above the focal plane where the potential well corresponds to the minimum irradiation intensity along the propagation axis.

The equilibrium position in the axial direction is determined by the counterbalance between the gravitational downward force $F_{mg} = mg$ and the photophoretic and light-pressure forces induced by the beam: $F_{\mathrm{rad}} + F_{\mathrm{PP}} = mg$, where m is the mass of the particle, and g the acceleration due to gravity. The levitating forces are recovered from the known mass and the size of the particle suspended at a particular equilibrium position in the diverging beam. We note here that both forces F_{rad} and F_{PP} acting on the illuminated surface are linearly dependent on laser intensity. In addition to both light-induced forces, buoyancy can potentially play a role in particle levitation, depending on the particle size and mass. For 2- and 20-μm solid-carbon particles, the forces exerted by buoyancy at atmospheric pressure are approximately 5×10^{-17} N and 5×10^{-14} N, respectively, whereas the gravitational forces are on the order of 10^{-13} N and 10^{-10} N; i.e., the former are 3 orders of magnitude smaller. Buoyancy will, therefore, be neglected in all further considerations. We note that the particles are always denser than a gas by orders of magnitude in case of solid particles and hollow spheres with a thin shell.

The stiffness of the trap in the transverse plane is determined from thermal motion of the particles observed with a fast CCD camera. The entire setup is contained within a vacuum chamber to conduct the experiments over a broad range of air pressures.

A linearly polarized Gaussian beam emitted from a continuous-wave (CW) laser of wavelength $\lambda = 532$ nm (Coherent Verdi V5) is converted into a single-charge vortex beam with a doughnut-shaped intensity cross section using a 16-step radial phase plate (Holo/Or) [Fig. 2(a)]. The incident beam with a doughnut mode is directed upward and focused with a 10× microscope plan achromat objective (Mitutoyo Plan APO 10x) with NA = 0.28, focal length $f = 20$ mm, and working distance of 33.5 mm. The radius of the vortex ring, i.e., of the maximum-intensity ring, in the focal spot $w_1 = w_0/\sqrt{2}$ is approximately 2.2 μm. Here, $w_0 = 3.1$ μm is the beam waist of a Gaussian beam. Beyond the Rayleigh range of $z_0 = \pi w_0^2/\lambda = 56$ μm, the beam diverges with a half-angle $\theta = 3.1°$ so that the radius of the doughnut beam r_b changes with distance z from the focal plane as $r_b = w_1[1 + (z/z_0)^2]$ [see Fig. 2(b)].

The displacement of a trapped particle in the transverse plane from the axis induces an asymmetry in the intensity distribution on the surface of that particle [Fig. 2(c)]. The irradiation asymmetry creates a net restoring photophoretic and light-pressure forces, pushing the particle back to the axis. For small displacements, the restoring force is linear.

The radiation pressure $\Omega_{\mathrm{rad}} = (1 + R)I/c$ is caused by the momentum transfer from photons, where R is the reflectivity, I is the laser intensity (power/area), and c is the speed of light. The force exerted by the CW laser beam on the particle is $F_{\mathrm{rad}} = \int \Omega_{\mathrm{rad}} dS$, where S is the spherical surface area illuminated by the beam. For example, focusing a power of 10^{-3} W into an area of 1 μm^2 results in an intensity of approximately 10^5 W/cm^2 and yields a radiation-pressure force of $F_{\mathrm{rad}} \sim 3$ pN, as given in Fig. 1.

2. Intensity distribution over a spherical surface

Both forces F_{rad} and F_{PP} are governed by irradiation intensity on the particle surface. The intensity distribution across the vortex beam with first topological charge $l = 1$ is given by [22]

$$I(r,z) = P_{\mathrm{tot}} \frac{r^2}{\pi w_1^4 \xi^2} \exp\left(-\frac{r^2}{w_1^2 \xi}\right), \qquad \xi = \left(1 + \frac{z^2 \lambda^2}{4\pi^2 w_1^4}\right), \tag{1}$$

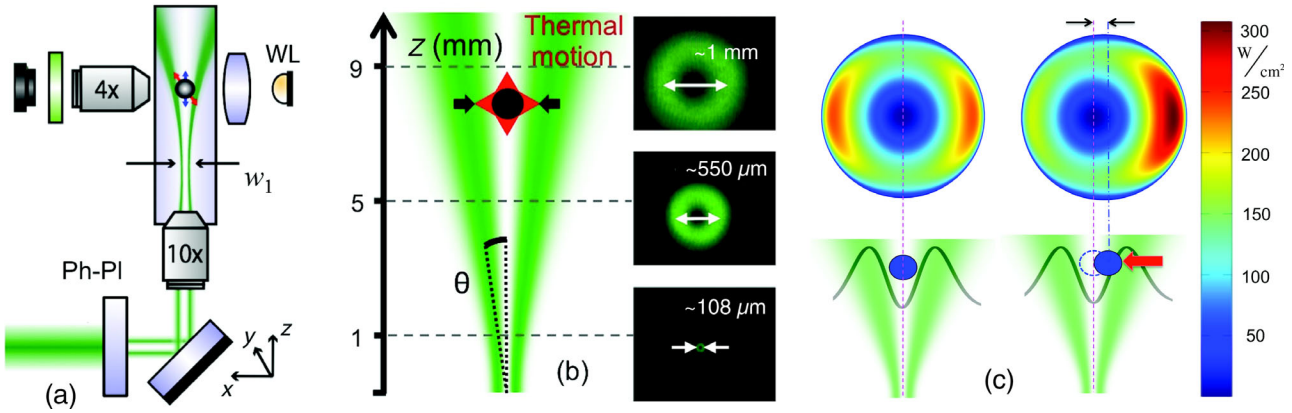

FIG. 2. Levitating particles in a diverging vortex beam. (a) Experimental setup of "optical nanoscales," Ph-Pl is the phase plate to form a vortex beam, 10× is a microscope objective to form the optical funnel, 4× is the microscope objective to track particle motion illuminated by white light (WL), and w_1 is the vortex beam waist. (b) The measured profile of the doughnut-shaped vortex beam and the cross sections $2r_b$ at various distances from the focal plane. (c) Two cases of calculated intensity distribution over a 5-μm particle located approximately 1 mm above the focus and projected on the y-z plane; the left one is for a particle on the z axis, and the right is for a particle shifted 1 μm away from the z axis. The polarization is horizontal, and the offset is in the direction of this polarization. The absorbed laser intensity on the particle surface is calculated for the total beam power of 1.0 W; the particle-to-vortex-size ratio is 1:20.

where r and z are radial and axial coordinates, P_{tot} is the total laser power in the beam, and w_1 is the waist of the vortex beam. To create an optical funnel with a controlled beam expansion angle, we focus the beam with a lens with focus f. The angle of the cone of the funnel is $\theta' = \theta_0 M$, where θ_0 is the Gaussian beam divergence, and M is the magnification of the focusing lens [Fig. 2(b)].

The force acting on a spherical particle with radius r_p illuminated by a vortex beam is determined by the axial component of the intensity at each point of the particle surface, which can be found using Fresnel equations separately for the s and p components [23]

$$I_{\mathrm{absorbed}} = I[|\vec{e}_s|^2 A_s + |\vec{e}_p|^2 A_p]\cos\theta_i, \tag{2}$$

where $\vec{e}_s$ and $\vec{e}_p$ are the s and p components of the incident laser field on a point on the spherical particle, θ_i is the polar angle of incidence, and $A_{s,p} = 1 - R_{s,p}$ are, correspondingly, the Fresnel absorption and reflectivity for the two components. An example of calculations of the absorbed laser-intensity distribution over the sphere positioned at the axis and shifted from the axis is presented in Fig. 2(c) for a 1:20 particle-to-vortex-radius ratio.

3. Photophoretic force in continuum flow and in free-molecular regimes

A number of analytical approaches have been developed to predict the dependence of photophoretic force F_{PP} on gas pressure p in both the continuum and free-molecular-flow regimes. In the free-molecular-flow regime ($\mathrm{Kn} \gg 1$), the force is the result of gas molecules scattering independently from the particle after having "accommodated" briefly at the surface. The translational kinetic energy of the gas molecules changes during this process, giving rise to a net force [13]

$$F_{\mathrm{PP}}^{\mathrm{Kn}\gg 1} = \frac{D r_p^2}{2\kappa_p}\left(\frac{p}{p^*}\right) I, \tag{3a}$$

where κ_p is thermal conductivity of the particle of radius r_p, and $p*$ is a characteristic pressure:

$$p^* = \frac{3}{\pi} D \frac{T_{\mathrm{gas}}}{r_p}. \tag{3b}$$

D denotes a constant determined entirely by the state of the gas,

$$D = \frac{\pi}{2}\sqrt{\frac{\pi}{3}}\kappa\frac{\bar{c}\eta}{T_{\mathrm{gas}}}, \tag{3c}$$

where κ is a thermal creep coefficient, $0.9 < \kappa < 1.14$ [13], $\bar{c}$ is the mean speed of the gas molecules, $\bar{c} = \sqrt{8RT_{\mathrm{gas}}/\pi M_{\mathrm{gas}}}$, R is the universal gas constant, M_{gas} is the molar mass, and η is the dynamic viscosity of the gas.

In the continuous-flow regime $\mathrm{Kn} \ll 1$, i.e., at high pressures, tangential temperature gradients in the gas flow cause a tangential flow velocity. This is the so-called thermal creep effect, which arises in a thin gas layer adjacent to the surface of the particle. The force can be expressed as [13]

$$F_{\mathrm{PP}}^{\mathrm{Kn}\ll 1} = \frac{D r_p^2}{2\kappa_p}\left(\frac{p}{p^*}\right)^{-1} I, \tag{4}$$

where D and $p*$ are given by Eqs. (3b) and (3c). In both regimes, the photophoretic force is proportional to the illuminating intensity. Taking again the example of a 1-μm-diameter graphite particle illuminated at atmospheric pressure by a 1-mW laser beam from a laser pointer focused to 1 $\mu\mathrm{m}^2$ on the particle surface to produce a laser intensity of 10^5 W/cm^2 ($\bar{c} = 493$ m/s at 20 °C, $\eta = 17.8$ μPa s in air), the resulting photophoretic force is $F_{\mathrm{PP}} \sim 275$ pN or approximately 75 times higher than the force of radiation pressure and approximately 25000 times higher than the force due to gravity (see above). We take the thermal conductivity of amorphous carbon 6.3 W/(m K), which is quite low when compared to metals, for example. A gold-coated surface illuminated by a 532-nm beam in the same conditions will experience $F_{\mathrm{PP}} \sim 1$ pN due to high thermal conductivity $k_{\mathrm{Au}} = 318$ W/(m K) and sufficient reflectivity approximately 0.8 at this wavelength.

B. Calibration of levitation forces in the optical funnel

The balance of force in the optical levitating nanoscale trap depends on the total laser power of the beam and on the intersection of the beam by the particle, as well as the environment pressure. The optical force varies along the z axis for a particle with given radius. Thus, calibration of forces in the trap at a fixed total laser power in the beam is conducted by measuring the equilibrium position of the particle relative to the focal plane and characterized by the ratio of the particle radius to the vortex beam radius w_1. This ratio is used to determine the illumination of the particle at its equilibrium position. We characterize the optical trap by measuring the equilibrium positions of 64 different particles of various sizes in the beam and conduct measurements at different cross sections by varying the laser power for a single particle trapped in the beam. The known mass of the particle allows us to recover the optically induced force in the axial direction while measuring the stiffness of trapping and the root-mean-square displacement from the axis yields the force in the transverse cross section of the beam.

1. Mass of glass shells

To calibrate the forces in the optical funnel, we use two types of particles with known masses and record the vertical positions of those particles in the funnel for various

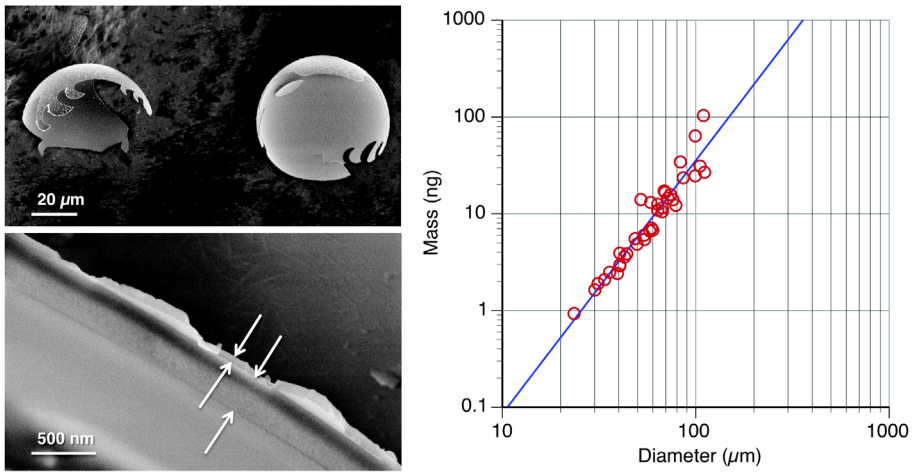

FIG. 3. Measurements of the shell mass. (a) SEM images of crashed glass shell of 56.8 μm in diameter (top) with the glass wall thickness of 350 nm and graphite coating 65-nm thick shown in the bottom image. (b) The dependence of the shell mass used in our experiments on the shell diameter. The solid line is the power fit of the shell mass m_p to the shell diameter $m_p \propto (2r_p)^{2.6\pm0.12}$.

laser powers and air pressures. We use solid graphite spheres of $2r_p$ in the range 2–12 μm (Sigma Aldrich no. 484164) for the beam characterization close to the focal plane and glass shells (K1, 3M Scotchlite) coated with a (30–100)-nm graphite layer with diameter ranging from 10 to 100 μm to calibrate forces farther away from the focus. The mass of the graphite spheres is evaluated by measuring the size and taking the graphite density 2.26 g/cm^3. In order to determine the mass of the glass shells, we crush a number of shells under the optical microscope and measure the wall and the coating-layer thickness under field emission scanning electron microscope. The result of mass dependence on the shell thickness is presented in Fig. 3. The mass of the shells varies between 1 and 100 ng, the diameter-to-mass relationship fits the power law $m_p \propto (2r_p)^{2.6\pm0.12}$, where m_p is in nanograms and r_p is in micometers. The density of the glass shells varies in size from approximately 0.05 to 0.5 g/cm^3 depending on the shell thickness. We note here that while the size of a particle reasonably accurately predicts the mass, thermal properties, which determine the photophoretic force, may vary due to variation in the graphite-coating thickness.

Particles are inserted into the diverging beam by picking them up with a brush dipped into a vial with samples and repeatedly flicking them from the brush over the top of a glass cylinder that encloses most of the trapping volume [Fig. 2(a)]. The glass enclosure protects the trap from convective flows in the lab, which otherwise will render the trap extremely unstable when not under vacuum. Once captured within the diverging conical funnel, particles find an equilibrium position as in a potential well and quiver around it due to Brownian motion, fluctuations in beam-pointing stability, and variation in laser intensity.

2. *Transverse trapping and axial levitating forces*

To reveal the elastic constant of trapping or the stiffness of the trap k (N/m), we follow well-established methods [19] by tracking a back-illuminated particle's position imaged onto a calibrated CCD (DALSA Genie HM640) at frame rates of approximately 2 kHz. The power spectral densities of these position time series show a distinctive dampening of the oscillations with an associated corner or knee frequency, which can be related to stiffness (see Fig. 4). Measurement of the transverse root-mean-square displacement of the particle from the average position $\langle x - \bar{x} \rangle$ can, thus, be related to average force $k\langle x - \bar{x} \rangle = \langle F \rangle$, where the average is taken over many thousands of position measurements recorded at a high frame rate [19,37–39]. Additionally, the tracking scheme measures the size of the particle, and, therefore, axial force can be recovered by knowledge of the size and lateral equilibrium position of the particle and determined from balance against gravity.

In order to accurately track the motion of particles, we passively improve the beam-pointing stability of the optical setup to a standard deviation <25 nm. As this standard deviation is orders of magnitude below the motion particles undergo while trapped, we can safely neglect the notion of beam-pointing instabilities in our further considerations. The laser intensity of our Verdi V5 varies <1% of output power and can be neglected as well. Given that the absorbing nature of our particles causes them to repel from high-intensity regions of the laser beam, a particle within the donut mode, or at least close to the central axis, acts as a harmonic oscillator, as it experiences a restoring force linearly proportional to the displacement from the central axis—the dark core. The power spectral density, which represents the mean-square deviation of the particle from the equilibrium in the frequency domain, is used in optical trapping for measuring the trap stiffness.

The particle equilibrium position observed in our experiments is typically in the range of 500 to 1200 μm above the focus of the beam, with an average particle size around 10 μm. The results of the particle motion in the trap are shown in Figs. 4 and 5. The crossover point, which determines the trap stiffness, is given by the intersection of the frequency-independent oscillation strength due

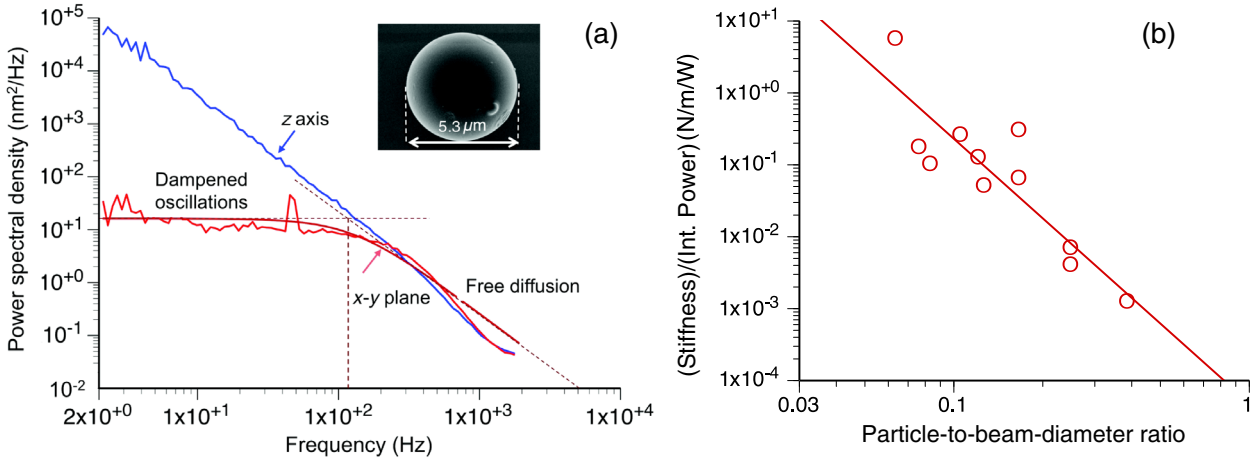

FIG. 4. Analysis of particle movement in the funnel trap at atmospheric pressure. (a) Example of a power spectrum of a motion of a graphite spherical particle 5.3 μm in diameter, trapped at atmospheric pressure in the potential well of an optical funnel in the transverse plane (red trace) and in the axial direction (blue trace). The inset shows the SEM image of the particle. The thick solid red line is a Lorentzian fit to the transverse position data, while the intersection between the free diffusion and damped oscillations (dashed lines) indicates the corner frequency, which determines the trap stiffness [19]. (b) The transverse stiffness of the trap normalized to the absorbed laser power recovered from experiments with particles trapped in various positions in the beam.

to trapping and a free-diffusion falloff. The transverse stiffness of the optical trap is dictated by both the total power in the trap and the geometry of the optical trap configuration. A small axial shift of the particle insignificantly changes only absorbed power; however, a transverse offset from the beam axis drastically increases absorbed power [see Fig. 2(c)]. The transverse root-mean-square (rms) forces normalized to the absorbed laser power are much larger than the normalized axial forces, as shown in Fig. 5.

With the particle in its equilibrium position within the dark core of the optical vortex, the trapping force is strongest at the points of steepest gradient in the illuminating intensity distribution, which are given by the two inner inflection points of the intensity distribution, so that $r_p/r_b = 0.5\sqrt{5-\sqrt{17}} \cong 0.468$, where r_b is the beam radius at the equilibrium position of the particle. Our experiments are conducted with a particle-to-beam-size ratio much less than 1. As this ratio decreases, the stiffness of trapping normalizes to absorbed power increases (see Fig. 5). We note that the absorbed laser power pushing the particle in the transverse plane is significantly lower than that in the axial direction. We use the power-law fit to the data to calibrate the light-induced force in the beam to enable the calculation of the trajectories of particles entering the beam at various velocities. Examples of mapping of forces in the beam at atmospheric pressure are presented in Sec. II D.

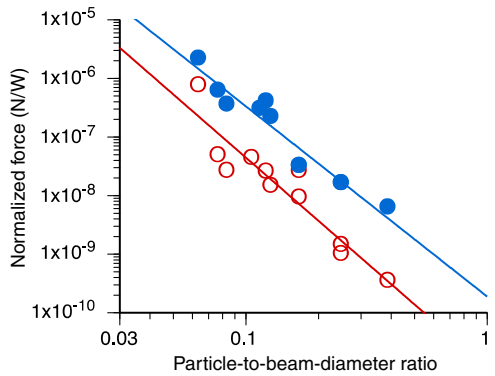

FIG. 5. Transverse rms trapping force (hollow red circles) and axial levitating force (filled blue circles) normalized to the absorbed laser power recovered from the measurements of trapping stiffness in the transverse plane and by taking the mass of levitating particles along the axis direction. The solid lines are a power-law fit to the experimental data.

C. Dependence of photophoretic force on the gas pressure

Varying the gas pressure changes the photophoretic force and subsequently moves the particle to a new equilibrium position, at which the laser-illumination distribution over the particle surface and the particle-to-beam size also changes in the optical funnel configuration. In order to uncover the dependence of photophoretic force on the gas pressure, we perform the following experiment: While varying the pressure in the chamber, we subsequently vary the laser power to keep the particle in the same position and, thus, preserve the illumination geometry. The pressure in the chamber is changed from 2 bar down to atmospheric pressure and further down to approximately 5 mbar. As the pressure decreases down to 100 mbar, the particles move to a higher position due to the increased photophoretic force. This holds down to around 20–100 mbar, where a transition from the continuous-flow to free-molecular-flow regime

takes place. Further decreases of pressure, consequently, require a reduction of the laser power to return the particle to the initial position with the initial particle-to-beam ratio.

Several graphite-coated glass shells with mass between 0.2 and 0.8 ng, size from 3 to 11 μm, and with various particle-to-beam-size ratios are used to build the experimental curve in order to check the dependence of the axial force imposed by the particles at different cross sections of the diverging laser beam; see Fig. 6.

We observe a linear relationship between the gas pressure above 100 mbar and the trapping power required to levitate a specific particle at a constant position. The experimental data deviate slightly from this linear dependence above atmospheric pressure, which most probably indicates the increase of temperature of the laser-irradiated particle and the surrounding gas and the resulting reduced temperature difference across the particle. According to Eq. 3(b), the maximum should occur at 29 mbar, which is in agreement with this observation. The transitional region where the photophoretic force goes through its maximum is clearly seen between 10 and 100 mbar. Below 10 mbar, the photophoretic force goes down with pressure, which requires higher laser power to keep the particle in a stable position (compare with Fig. 1).

D. Map of forces in the optical funnel

The linear relationship between the levitating force and the required beam power for different particle sizes and at different positions in the beam suggests a linear

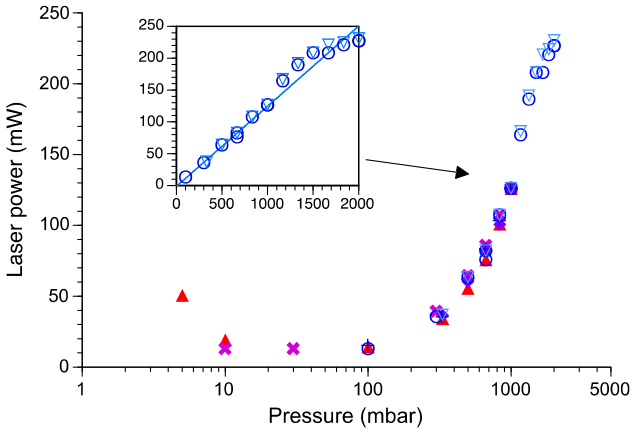

FIG. 6. The relation between the gas pressure and the laser power required to keep the particle in a constant equilibrium position in the diverging beam. The curve is composed of measurements of six particles with different mass and at the following r_p/r_b ratios in their equilibrium positions: $r_p/r_b = 0.8$ (red triangles), 0.11 (blue diamonds), 0.12 (blue circles), 0.12 (blue inverted triangles), 0.13 (blue crosses), 0.22 (bold purple crosses). The transitional regime in the (10–100)-mbar range is clearly observed. The characteristic pressure for a 10-μm particle in nitrogen is $p* = 29$ mbar. The linear dependence above 100 mbar is shown in the inset.

dependence of the levitating force on the illuminating intensity. Strictly speaking, this linear model is valid only for small enough deviations from the axis for Hooke's law to be valid. In this simple picture, we assume that the transverse force on a particle is proportional to its offset up to the inner inflection point of the beam profile, at which the force attains its maximum. With larger deviations, the force decreases again linearly up to the maximum of the laser-beam intensity distribution, where it goes to zero. The calibration of forces recovered from the experimental data shown in Fig. 5 yields calibration curves which link axial and transverse forces as well as stiffness of the trap to the position of the particle in the optical funnel. The obtained dependences normalized to the illuminating laser power allows us to extrapolate the forces acting on any particle within the entirety of the beam geometry.

The power absorbed on a graphite or graphite-coated particle at any given point within the beam is given as the surface integral over Eq. (2). The magnitude of the axial force is then the absorbed power times the scale factor of the calibration obtained above (Fig. 5). The only fixed parameters of the calibration are the thermal and optical properties of the particle and the gas pressure. Forces within arbitrary beam geometries can be derived by calculating the absorbed power from the intensity distribution in the beam. In our simple model, we assume the force to be linear with increasing offset from the axis with the proportionality constant given by the recovered stiffness.

The resulting maps of absorbed power to axially and transversely directed forces exerted on a 1-μm-diameter light-absorbing particle by a 5-W beam are presented in Figs. 7(a) and 7(b). The stable equilibrium position is on the axis. The more a particle is shifted away from the axis to the ring of the vortex beam, the higher the illuminating intensity, and, thus, the higher the force, both in axial and transverse directions. The axial force applied to a light-absorbing particle is always directed upward, in the direction of beam propagation [Fig. 7(a)]. As long as the absorbing particle remains within the "doughnut" ring, the force points upwards and toward the beam axis, and the overall force has its maximum at the maximum intensity of the ring. As the particle passes through the vortex ring, the illumination and the axial force gradually reduce to zero at the periphery of the beam profile.

Similar to the axial case, the inward-pointing returning force gradually increases with offset. In contrast to the axial case, however, maximum force on the particle is reached at the inflection points of the potential, i.e., where the flanks of the vortex profile are steepest. As long as a particle remains "inside" the vortex, the force points inwards, up to the equilibrium point which is located at the maximum-intensity ring of the vortex profile. Farther outwards, the force reverses direction and gradually increases in magnitude, so the particle is propelled outwards.

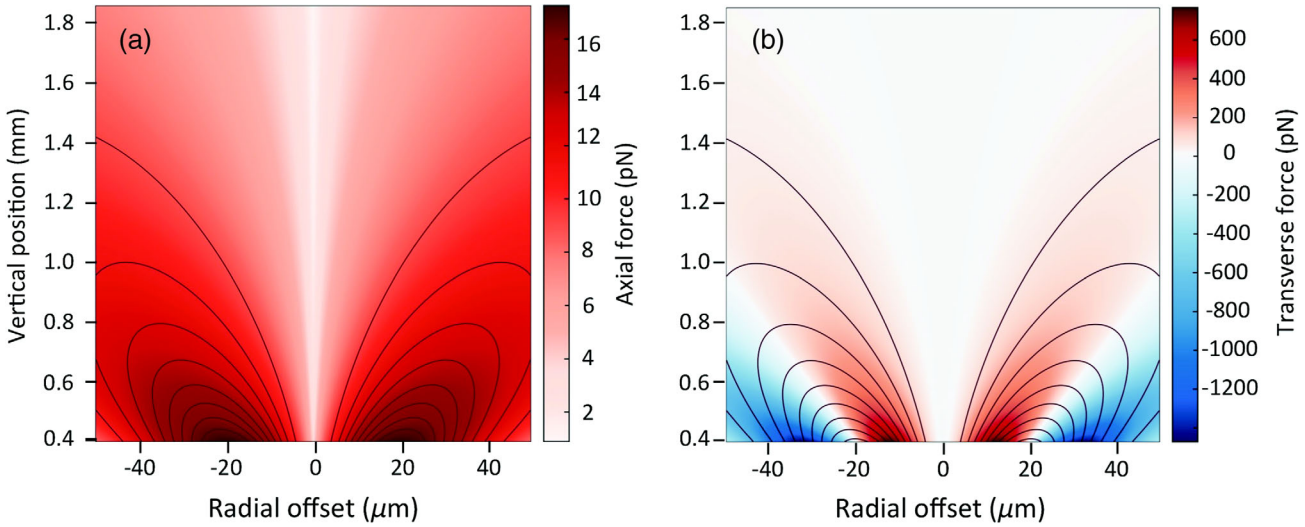

FIG. 7. An example of the map of force imposed on a 1-μm-diameter particle by an upward propagating diverging doughnut-shape 5-W beam with geometry as in Fig. 2, determined by calibration. (a) The axial component of the force; the maximum axial force occurs at the ring of maximum intensity of the laser beam. (b) The transverse component of the same force. Here, positive (red) indicates a force directed radially inwards and negative (blue) radially outwards. In contrast to the axial case, the highest inward-directed force is at the maximum of the intensity gradient, i.e., at the inflection points on vortex beam profile. Note the difference in the color scales in (a) and (b).

The results of the mapping can be used to calculate particle trajectories and determine the required laser-beam configuration and beam power for particle injection. An example of such calculation is presented in the following section.

III. PARTICLE TRAJECTORIES IN AN OPTICAL FUNNEL

To further our understanding of the beam geometries and laser powers required to achieve good confinement of particles entering the diverging counterpropagating beam funnel, we use the mapping of the absorbed laser power to effective force as obtained above in Fig. 7. In order to simulate the trajectories, we consider, for the sake of simplicity, fully absorbing micrometer-size particles at atmospheric pressure with waterlike density, which is common for many biological samples, injected into the funnel at various distances from and parallel to the optical beam axis.

A. Particle trajectories: The frictionless case

To calculate the trajectories, we consider particles entering the laser field in free flight parallel to the beam axis, without significant transverse velocity components. The equations of motion are given by the coupled system

$$\begin{cases} m_p \frac{\partial^2 x}{\partial t^2} = F_x(x(t), z(t)), \\ m_p \frac{\partial^2 z}{\partial t^2} = F_z(x(t), z(t)) - m_p g, \end{cases} \tag{5}$$

where $F_{x,z}$ are the transverse (x) and axial (z) components of the force field calculated with the model described in the previous section, and $g = 9.8\ \mathrm{m/s^2}$ is a free-fall acceleration. We do not consider friction due to the gas viscosity here. We set the following conditions for these computations: The particles enter the interaction region 30 mm from the focal plane of the optical funnel, parallel to the beam axis, the radius of beam waist is $w_1 = 2.5\ \mu$m, the divergence is $\theta' = 3.1°$, as described in Sec. II A 1, and the total laser power in the beam is 5 W. We then vary the offset of the initial particle position from the optical axis for particles with a fixed entrance speed of 15 m/s [Fig. 8(a)] and vary the particle speed for a fixed offset of 10 μm [Fig. 8(b)].

As can be seen from the figures, the particle with initial speed of 15 m/s injected with impact parameters (defined as a radial distance from the axis) of 5 and 10 μm are deflected inwards and directed to the focal point inside a 2.5-μm ring of the funnel waist. However, the particle injected with a 20-μm impact parameter penetrates the funnel wall and is deflected farther away from the axis. Particles entering the interaction region within the 2.5-μm waist of the vortex ring and parallel to the funnel axis will pass through the "focal area" of the beam unaided and are considered "trapped" regardless of the trapping laser.

Figure 8(b) shows the traces for the same particle entering the trap at a fixed impact parameter of 10 μm but with various speeds. The particle entering with 30 m/s penetrates the trap and deflects farther away from the axis, while the slowest one with 10 m/s is axially reflected from the trap at about 1 mm above the focal plane. The speed range for which the particles reach the focus is 12–20 m/s, with the particle moving with 15 m/s goes straight into the focus of the trap. The 12-m/s particle oscillates around the

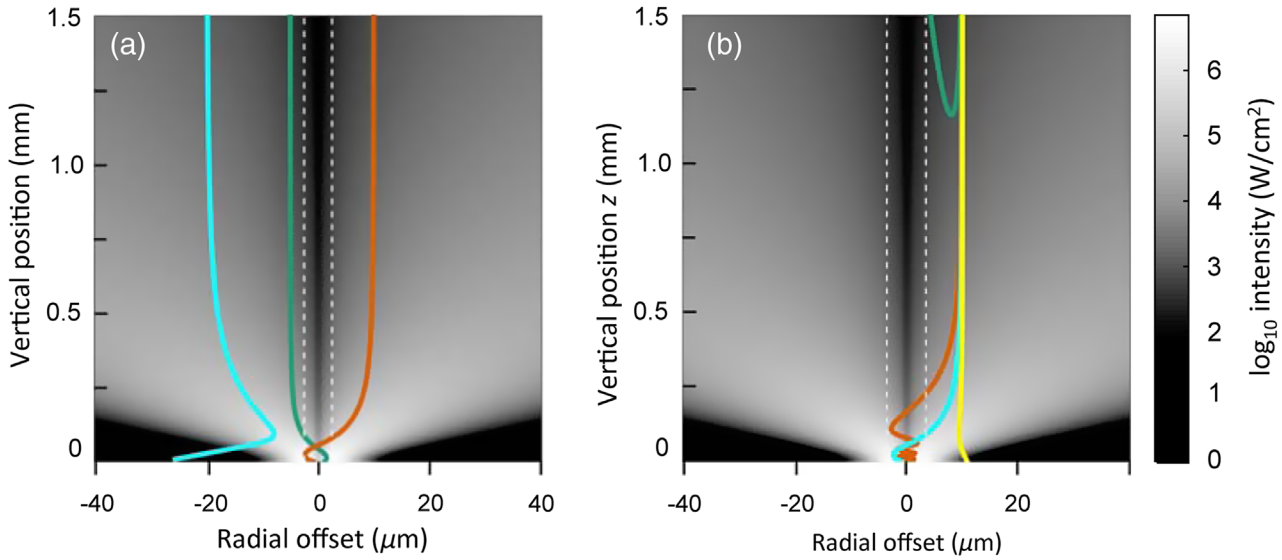

FIG. 8. (a),(b) Examples of the calculated trajectories for a 1-μm particle entering the optical funnel with a total laser power of 5 W. The dashed lines show the size of the vortex ring in the focus of the beam; the scale on the right shows the logarithm of laser intensity illuminating the particles in various points of the beam. (a) Trajectories of particles entering the trap with a speed of 15 m/s at a transverse offset of 5 μm (green), 10 μm (red), and 20 μm (cyan). While the first two are reliably trapped and directed to the focus, the particle starting at 20 μm penetrates through the ring of maximum intensity and escapes the 2D trap. (b) Trajectories of particles entering at a fixed offset of 10 μm from the axis with the initial speed of 10 m/s (green), 12 m/s (red), 15 m/s (cyan), and 30 m/s (yellow). The slowest particle is decelerated axially to a full stop by the trapping beam before entering the focal area and then propelled away upwards. The fastest is deflected away to escape the trap. The particles with intermediate speed are trapped in the core of the beam and pass through the focus inside the doughnut.

axis in the "neck" of the optical funnel and, thus, spends a much longer time in the focal area, reaching up to millisecond residence times in the focal area, while the 20-m/s particle passes through the 5-μm focus in just 0.25 μs. Slowing the particles confined to the focal area is the ideal case to achieve in the coherent x-ray diffractive imaging experiments when x-ray pulse rates are limited. On the other hand, at future XFEL sources that operate at megahertz-pulse-repetition rates, it is, instead, advantageous to maintain velocities of about 10–100 m/s in order to avoid preexposure to the x-ray beam or debris from other interacting particles, prior to the time at which particles reach the focus.

The deflection of the particle depends strongly on the laser power of the trapping beam. For example, a laser power of 1 W is not sufficient to trap a 1-μm particle moving at 15 m/s; it is deflected outwards after piercing through the high-intensity wall of the doughnut beam. At higher laser powers, the particle is deflected inwards and oscillates in a dampened motion around the dark core. With further increase of laser power, the particle deflects from the trap without entering the focal area.

In order to summarize the parameters required to achieve confinement of fast-moving light-absorbing particles in our trap, we label a particle as trapped when it passes through the focus of the laser beam within the vortex beam, i.e., like the red trace (10-μm offset) in Fig. 8(a) and the cyan trace ($v_z = 15$ m/s) in Fig. 8(b). The results of searching the parameter space for trapped particles are shown in Fig. 9.

The parameter space is at least four dimensional. It includes particle speed, offset, velocity, laser power, and can include further parameters, for example, initial transverse momentum, optical absorptivity, gas pressure, and particle density. The lowest boundary of each contour shows a floor of initial velocities where particles are no longer trapped due to deceleration to a full stop and ejection upwards out of the trap without reaching the focal plane, as shown in Fig. 8(b). The boundary also shows the maximum initial velocity for each particular initial offset for the trapped particles. The visible "ceiling" is the upper limit of particle momenta that can successfully be trapped. The particles entering the interaction region within the waist of the vortex ring of 2.5 μm are trapped regardless of the presence of the trapping laser. The presented results show that small particles are much easier to confine, even at higher speeds, as their momentum $m_p v_z$ is much smaller. The larger the aerosol particles, the more selective the trap is in terms of initial velocities of particles that are successfully trapped. Compare the phase-space areas circumscribed by the contours in the left and right panels in Fig. 9, for example.

The parameter space can be used to evaluate the efficiency of the trap. Taking particles of size 1 μm traveling at 15 m/s in the beam geometry shown in Fig. 8(a) and using the full available laser power of 5 W, we see from Fig. 8 that the radial distance at which we can successfully capture particle is approximately 11 μm, a 4.4-fold increase over the approximately 2.5 μm distance considered as trapped in

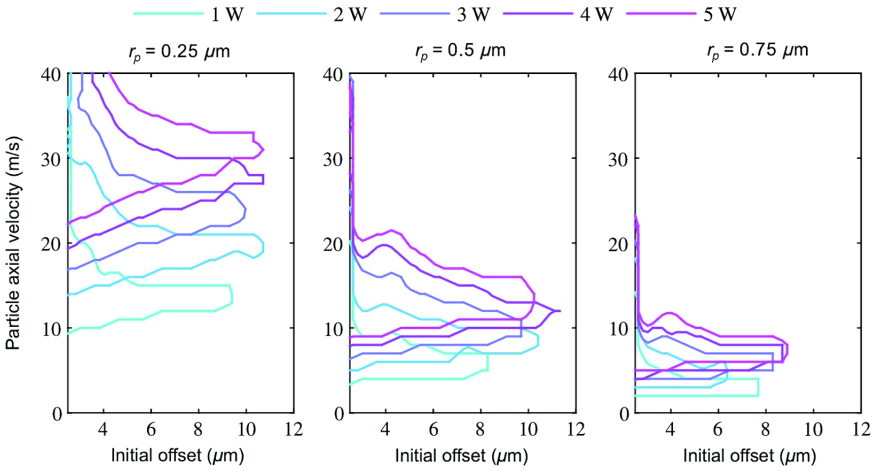

FIG. 9. Parameter-space-acceptance plots for three particles with diameters of 0.5, 1.0, and 1.5 μm, respectively, entering the beam geometry presented in previous figures. The contour color indicates laser power increasing in five steps from 1 W (cyan) to 5 W (magenta). The areas inside the contours (to the left of the lines) indicate particles that are deflected into the interaction region, i.e., within the size of the 2.5-μm waist of the vortex ring and are considered trapped.

the absence of the trapping beam. The particle confinement within the optical funnel yields an approximately twentyfold increase in achievable particle density. Moreover, it suggests orders of magnitude reduction in particle speed, which is very desirable in many potential applications such as x-ray morphology of particles by diffraction scattering.

B. Particle trajectories considering the effect of air friction

Friction appears only when the particle has a different speed relative to the gas. In an aerosolized jet of particles moving at the same velocity as the carrier gas, friction or drag is negligible. After exiting an aerosol injector into vacuum, where the carrier gas expands and reaches approximately sonic speeds, particles typically cease to accelerate due to reduced pressure and, hence, reduced drag. However, in some cases, drag forces may play a major role in the trajectory of a particle. As an example, we consider the case in which particles are injected into a gas with no net velocity. The terminal velocity v_t for particles falling freely under the gravitation force is then given by Stokes's law

$$v_t = \frac{2}{9}\frac{(\rho_p - \rho_g)}{\mu} g r_p^2, \tag{6}$$

where ρ_p, ρ_g are the density of particle and gas, respectively, and μ is the dynamic gas viscosity. For air with a viscosity of $\mu_{\text{air}} = 18.6$ μPa s at atmospheric pressure and for 0.5- and 5-μm-radius particles, the terminal velocities are 0.3 and 30 mm/s, correspondingly. The equations of motion are now

$$\begin{cases} m_p \frac{\partial^2 x}{\partial t^2} = F_x(x(t), z(t)) + 6\pi\mu r_p \frac{\partial x}{\partial t}, \\ m_p \frac{\partial^2 z}{\partial t^2} = F_z(x(t), z(t)) + 6\pi\mu r_p \frac{\partial z}{\partial t} - m_p g. \end{cases} \tag{7}$$

The trajectories for a particle injected into the funnel with initial speed of 3 mm/s at various distances from the beam axis are shown in Fig. 10. The laser power in the beam is 5 W, and the intensity distribution in the optical funnel is the same as in Fig. 8. The linear relationship of drag force and particle velocity completely dampens the oscillations observed in Fig. 8. The particles are unable to "fall" through the focus, and the drag force limits the particle momentum to such values that the particles are unable to pierce through the trap as observed in the frictionless case. The particle simply falls into the funnel, and, after deceleration caused primarily by drag forces, is guided along the contours of the laser beam where gravity is counterbalanced against the vertical optically induced forces. The particle moves along this contour until reaching its equilibrium position above the laser focus, where both vertical and transverse forces are balanced.

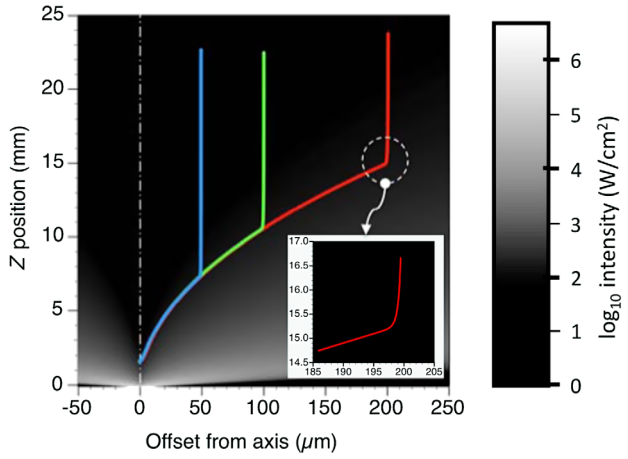

FIG. 10. Particle trajectories calculated in air at atmospheric pressure taking into account drag force in a 5-W optical funnel with intensity field as in Fig. 8. A 5-μm-radius particle enters the light field at its terminal velocity for a range of initial offsets away from the axis of 50 μm (blue), 100 μm (green), and 200 μm (red). The inset shows the magnified area where the vertical speed of particle dropped down to approximately 0.1 mm/s, and the particle starts accelerating toward the beam axis. Note that for better visibility, the vertical scale is in millimeters, and the radial offset is in micrometers.

IV. CONCLUSIONS AND OUTLOOK

The conducted series of experiments demonstrates that optical trapping with optically induced photophoretic forces in gaseous media is developing from a proof-of-principle concept into a powerful quantitative tool for touch-free diverging and focusing jets of particles in a desirable and predicted manner. We develop a funnel-shaped optical levitation trap and calibrate optical forces in the trap depending on laser intensity and beam geometry. The results of a quantitative analysis of the photophoretic force and the stiffness of trapping achieved by levitating graphite and carbon-coated glass shells of calibrated sizes in an upright diverging hollow-core vortex beam show the possibility to divert and focus a jet of particles into a desirable location with micrometer-scale precision. Mapping of forces to a particular intensity distribution in the beam allows us to build a parameter space for focusing a jet of particles depending on particle size, speed, offset, velocity, and laser power. This can be further extended to include, for example, initial transverse momentum, optical absorptivity, gas pressure, and particle density.

Our first proof-of-principle measurements of optical forces acting on a particle in the optical funnel are very encouraging. However, there are several obstacles to be resolved to perform predictable manipulation of particle streams with optically induced forces. One of those is determining the maximum laser intensity on the particle surface, which directly relates to the maximal force that can be applied to a particular particle with certain optical and thermal characteristics on the one hand and to the maximum permitted temperature on the particle surface.

Let us estimate the maximum laser intensity that can be applied, as an example, to a 1-μm graphite particle in air at atmospheric pressure, as used in our calibration experiments. The obvious limitation is that the absorbed laser energy should be below the level at which the particle can be destroyed or change its physical or chemical property or its structure. Graphite sublimates at temperatures around 3600 °C in vacuum [40]; however, when exposed to air, the activation energy for oxidation is 167 kJ/mol at atmospheric pressure [41], so it combusts at temperature above 330 °C. The elevation of the average surface temperature T_s of a sphere in a continuous-flow environment with temperature T_{air} can be expressed as a function of the heat flux H_{cont} [13]:

$$H_{\mathrm{cont}} = 4\pi r_p k_g (T_s - T_{\mathrm{air}}) = 4\pi r_p k_g \Delta T. \qquad (8)$$

A solid 1-μm graphite sphere with thermal conductivity $k_g = 4.6\ \mathrm{W/(m\,K)}$ illuminated by the laser intensity of $I_{\mathrm{las}} = 10^5\ \mathrm{W/cm^2}$ will absorb $\pi r_p^2 I_{\mathrm{las}} = 785\ \mu\mathrm{W}$. If this power is entirely exchanged by collisions with gas molecules at atmospheric pressure, the particle surface temperature will elevate by $\Delta T = 27$ K. Reversing this calculation allows us to estimate the power required to be absorbed by the particle to elevate the temperature to 330 °C, i.e., by 300 K, which is 8.6 mW, or in terms of intensity,$1.1 \times 10^6\ \mathrm{W/cm^2}$. This value is valid in the entire continuous-flow regime. Because of the massive decrease in gas-particle interaction in the free-molecular-flow regime, the particle is effectively no longer cooled by the interaction and releases heat only as a radiating black body. The reduced heat dissipation limits the maximum allowed laser intensities at low pressures. We note here that laser-illuminated biological samples and macromolecules, which must not be overheated above, say, 50 °C, will require maximum allowable illuminating-laser intensities on the order of $10^5\ \mathrm{W/cm^2}$. However, one must consider the full trajectory, intensity profile, bioparticle absorption, and thermal-conductivity properties to know the limit where the overheating is a danger.

The obtained calibration of optical forces paves the way for two new key applications, namely, using the levitating trap as a weighing scale for masses in the nanogram and picogram range, and as an optical funnel, or even more advanced traps, for an aerosolized stream of microparticles in both vacuum and at atmospheric pressure. Using a calibrated weight with fixed optical and thermal properties, the weight of a particle can be determined by the axial equilibrium position established for the given laser power and ambient gas pressure.

We plan to use the optical funnel to enhance the efficiency of sample injection in structural morphology diffraction experiments conducted at free-electron-laser facilities. In order to support the operational requirements of free-electron-laser experiments, preferably working in high vacuum or in helium gas, our calibration can be extrapolated into the free-molecular-flow regime. The presented measurements combined with our modeling of particle trajectories in the optical funnel provides a promising pathway to guide micrometer- and submicrometer-size particles into the focal spot of an x-ray free-electron laser and to significantly enhance the hit rate and increase the efficiency of nanoscale morphology measurements of proteins and biomolecules in coherent diffractive imaging experiments [34].

The presented analysis of optical forces provides the basis for further optimization of the laser funnel beam in terms of intensity and angle of divergence for a particular particle size, speed, and the air pressure or vacuum environment, and for targeting specific particles utilizing their known optical and thermal properties. The latest developments in building complex laser-beam architectures by spatial beam modulators include controlled and spatially variant polarization states and profiles that change in time as a particle propagates through the trap. We believe that the possibilities for optical manipulation of particle streams in a gas environment are boundless.

ACKNOWLEDGMENTS

We thank E. G. Gamaly for fruitful discussions. This work is supported by the excellence cluster "The Hamburg Center for Ultrafast Imaging—Structure, Dynamics and Control of Matter at the Atomic Scale" of the Deutsche Forschungsgemeinschaft (DFG, Project No. EXC1074). This research is partially supported under Australian Research Council's Discovery Projects funding scheme (Project No. DP110100975). R. K. acknowledges support from the NSF Science and Technology Centers Award No. 1231306. J. K. acknowledges support from the European Research Council through the Consolidator Grant No. 614507-COMOTION. R. B. holds a Research Fellowship at Queens' College, Cambridge, UK.

[1] D. McGloin, D. R. Burnham, M. D. Summers, D. Rudd, N. Dewar, and S. Anand, Optical manipulation of airborne particles: Techniques and applications, Faraday Discuss. **137**, 335 (2008).

[2] D. R. Biurnham and D. McGloin, Modeling of optical traps for aerosols, J. Opt. Soc. Am. B **28**, 2856 (2011).

[3] V. G. Shvedov, A. V. Rode, Ya. Izdebskaya, A. S. Desyatnikov, W. Krolikowski, and Yu. Kivshar, Giant Optical Manipulation, Phys. Rev. Lett. **105**, 118103 (2010).

[4] Z. Zhang, D. Cannan, J. Liu, P. Zhang, D. N. Christodoulides, and Z. Chen, Observation of trapping and transporting airborne absorbing particles with a single optical beam, Opt. Express **20**, 16212 (2012).

[5] O. A. Schmidt, M. K. Garbos, T. G. Euser, and P. S. J. Russell, Metrology of laser-guided particles in air-filled hollow-core photonic crystal fiber, Opt. Lett. **37**, 91 (2012).

[6] A. Ashkin, Acceleration and Trapping of Particles by Radiation Pressure, Phys. Rev. Lett. **24**, 156 (1970).

[7] T. X. Phuoc, A comparative study of the photon pressure force, the photophoretic force, and the adhesion van der Waals force, Opt. Commun. **245**, 27 (2005).

[8] F. Ehrenhaft, On the physics of millionths of centimeters, Physik. Zeitschr. **18**, 352 (1917).

[9] E. J. Davis and G. Schweiger, *The Airborne Microparticle: Its Physics, Chemistry, Optics, and Transport Phenomena* (Springer-Verlag, Berlin, 2002), pp. 755–810.

[10] A. Melzer, Laser manipulation of particles in dusty plasmas, Plasma Sources Sci. Technol. **10**, 303 (2001).

[11] S. Beresnev, V. Chernyak, and G. Fomyagin, Photophoresis of a spherical particle in a rarefied gas, Phys. Fluids A **5**, 2043 (1993).

[12] H. C. Weng and C.-K. Chen, On the importance of thermal creep in natural convective gas microflow with wall heat fluxes, J. Phys. D **41**, 115501 (2008).

[13] H. Rohatschek, Semi-empirical model of photophoretic forces for the entire range of pressures, J. Aerosol Sci. **26**, 717 (1995).

[14] L. D. Reed, Low Knudsen number photophoresis, J. Aerosol Sci. **8**, 123 (1977).

[15] M. Esseling, P. Rose, C. Alpmann, and C. Denz, Photophoretic trampoline—interaction of single airborne absorbing droplets with light, Appl. Phys. Lett. **101**, 131115 (2012).

[16] H. He, M. E. J. Friese, N. R. Heckenberg, and H. Rubinsztein-Dunlop, Direct Observation of Transfer of Angular Momentum to Absorptive Particles from a Laser Beam with a Phase Singularity, Phys. Rev. Lett. **75**, 826 (1995).

[17] H. Rubinsztein-Dunlop, T. A. Nieminen, M. E. J. Friese, and N. R. Heckenberg, in *Advances in Quantum Chemistry: Modern Trends in Atomic Physics*, edited by P.-O. Lowdin (Academic Press, New York, 1998), Vol. 30, pp. 469–492.

[18] M. Woerdemann, C. Alpmann, M. Esseling, and C. Denz, Advanced optical trapping by complex beam shaping, Laser Photonics Rev. **7**, 839 (2013).

[19] R. W. Bowman and M. J. Padgett, Optical trapping and binding, Rep. Prog. Phys. **76**, 026401 (2013).

[20] M. Padgett and R. Bowman, Tweezers with a twist, Nat. Photonics **5**, 343 (2011).

[21] V. G. Shvedov, A. S. Desyatnikov, A. V. Rode, W. Krolikowski, and Y. S. Kivshar, Optical guiding of absorbing nanoclusters in air, Opt. Express **17**, 5743 (2009).

[22] A. S. Desyatnikov, V. G. Shvedov, A. V. Rode, W. Krolikowski, and Y. S. Kivshar, Photophoretic manipulation of absorbing aerosol particles with vortex beams: Theory versus experiment, Opt. Express **17**, 8201 (2009).

[23] N. Eckerskorn, N. Zeng, V. G. Shvedov, W. Krolikowski, and A. V. Rode, Effect of polarization on air-transport of particle by optical vortex beam, J. Opt. **14**, 055302 (2012).

[24] V. G. Shvedov, C. Hnatovsky, N. Eckerskorn, A. V. Rode, and W. Krolikowski, Polarisation sensitive photophoresis, Appl. Phys. Lett. **101**, 051106 (2012).

[25] V. G. Shvedov, A. V. Rode, Y. V. Izdebskaya, A. S. Desyatnikov, W. Krolikowski, and Y. S. Kivshar, Selective trapping of multiple particles by volume speckle field, Opt. Express **18**, 3137 (2010).

[26] V. G. Shvedov, A. V. Rode, Y. V. Izdebskaya, D. Leykam, A. S. Desyatnikov, W. Krolikowski, and Y. S. Kivshar, Laser speckle field as a multiple particle trap, J. Opt. **12**, 124003 (2010).

[27] V. G. Shvedov, C. Hnatovsky, N. Shostka, A. V. Rode, and W. Krolikowski, Optical manipulation of particle ensembles in air, Opt. Lett. **37**, 1934 (2012).

[28] F. Liu, Z. Zhang, S. Fu, Y. Wei, T. Cheng, Q. Zhang, and X. Wu, Manipulation of aerosols revolving in tapering optical traps, Opt. Lett. **39**, 100 (2014).

[29] P. Zhang, Z. Zhang, J. Prakash, S. Huang, D. Hernandez, M. Salazar, D. N. Christodoulides, and Z. Chen, Trapping and transporting aerosols with a single optical bottle beam generated by moiré techniques, Opt. Lett. **36**, 1491 (2011).

[30] V. G. Shvedov, C. Hnatovsky, A. V. Rode, and W. Krolikowski, Robust trapping and manipulation of airborne particles with a bottle beam, Opt. Express **19**, 17350 (2011).

[31] T. Čižmár, O. Brzobohatý, K. Dholakia, and P. Zemánek, The holographic optical micro-manipulation system based on counter-propagating beams, Laser Phys. Lett. **8**, 50 (2011).

[32] N. Eckerskorn, L. Li, R. A. Kirian, J. Küpper, D. P. DePonte, W. Krolikowski, W. M. Lee, H. N. Chapman, and A. V. Rode, Hollow Bessel-like beam as an optical guide for a stream of microscopic particles, Opt. Express **21**, 30492 (2013).

[33] O. A. Schmidt, M. K. Garbos, T. G. Euser, and P. S. J. Russell, Reconfigurable Optothermal Microparticle Trap in Air-Filled Hollow-Core Photonic Crystal Fiber, Phys. Rev. Lett. **109**, 024502 (2012).

[34] H. N. Chapman, P. Fromme, A. Barty *et al.*, Femtosecond x-ray protein nanocrystallography, Nature (London) **470**, 73 (2011).

[35] M. Bogan, S. Boutet, H. N. Chapman *et al.*, Aerosol imaging with a soft x-ray free electron laser, Aerosol Sci. Technol. **44**, i (2010).

[36] K. Ayyer, Gianluca Geloni, V. Kocharyan, E. Saldin, S. Serkez, O. Efanov, and I. Zagorodnov, Perspectives for imaging single protein molecules with the present design of the European XFEL, Struct. Dyn. **2**, 041702 (2015).

[37] G. M. Gibson, J. Leach, S. Keen, A. J. Wright, and M. J. Padgett, Measuring the accuracy of particle position and force in optical tweezers using high-speed video microscopy, Opt. Express **16**,14561 (2008).

[38] K. Berg-Sorensen and H. Flyvbjerg, Power spectrum analysis for optical tweezers, Rev. Sci. Instrum. **75**, 594 (2004).

[39] T. Čižmár, L. C. Dávila Romero, K. Dholakia, and D. L. Andrews, Multiple optical trapping, and binding: New routes to self-assembly, J. Phys. B **43**, 102001 (2010).

[40] R. Backreedy, J. M. Jones, W. Pourkashanian, and A. Williams, A study of the reaction of oxygen with graphite: Model chemistry, Faraday Discuss. **119**, 385 (2001).

[41] R. C. Weast and M. J. Astle, *CRC Handbook of Chemistry and Physics*, 60th ed. (CRC, Boca Raton, FL, 1981).